

Supplementary Material

Electrochemical Immunosensor for Antibody Recognition Against SARS-CoV-2 B-Cell Epitope: Impact of RBD Mutations on Antigen-Antibody Binding

Freddy. A. Nunez,^{a,b} Vivian L. de Oliveira,^{a,d,e} Cesar Remuzgo,^d Marcos R. de A. Silva,^a Isabela Daher,^{c,d} Jamille R. Oliveira,^{c,d} Tamires L. Silva,^{c,d} Edecio Cunha-Neto,^{c,d,e} Jorge Kalil,^{c,d,e} Keity S. Santos,^{c,d,e} Quinn A. Besford,^b Wendel A. Alves.^{a,*}

^a *Centro de Ciências Naturais e Humanas, Universidade Federal do ABC, Santo André, São Paulo 09210-580, Brazil.*

^b *Leibniz-Institut für Polymerforschung e.V., Hohe Str. 6, 01069 Dresden, Germany.*

^c *Departamento de Clínica Médica, Disciplina de Alergia e Imunologia Clínica, Faculdade de Medicina da Universidade de São Paulo, São Paulo 01246-903, Brazil.*

^d *Laboratório de Imunologia, INCOR, Hospital das Clinicas HCFMUSP, Faculdade de Medicina, Universidade de São Paulo, São Paulo 05403-900, Brazil.*

^e *LIM-19, Hospital das Clinicas HCFMUSP, Faculdade de Medicina, Universidade de São Paulo, São Paulo 05403-900, Brazil.*

*Corresponding author: wendel.alves@ufabc.edu.br

Table of Contents:

Supporting Text

1. Experimental section.....	S1
2. Optimization Assays.....	S3

Supporting Figures

- Figure S1.** Structure of the B38 antibody complexed with SARS-CoV-2 RBD. (A) Wuhan RBD (PB ID: 7BZ5), (B) Omicron RBD (PDB ID: 7XIK). The structure of the P44 peptide within the RBD structure is highlighted in red, and the residues that interact with the P44 peptide are shown in orange.....S5
- Figure S2.** P44 peptides' three-dimensional structure prediction. (A) P44 WT, (B) P44 Gamma, (C) P44 Omicron. In green is shown the β -turn, and in gray are shown random coil structures.....S5
- Figure S3.** Circular dichroism spectra of P44 peptides: (A) WT, (B) Gamma, and (C) Omicron.....S6
- Figure S4.** Crystallographic and morphological characterizations of the ZnONRs device: (A) X-ray diffraction spectra; (B) SEM image of the ZnONRs film; (C) detail of a single nanorod; (D) histogram of ZnONRs diameters.....S6
- Figure S5.** Mean fluorescence intensity values obtained by CLSM at each fabrication stage of the P44 WT immunosensor.....S7
- Figure S6.** SEM and CLSM images at different assembly steps of P44 Gamma and P44 Omicron immunosensors: (A) ZnONRs/APTES/GA/P44 Gamma; (B) ZnONRs/APTES/GA/P44 Gamma/BSA/mAb B38; (C) ZnONRs/APTES/GA/P44 Omicron; (D) ZnONRs/APTES/GA/P44 Omicron/BSA/mAb B38.....S7
- Figure S7.** Comparison of mean fluorescence intensity for P44 WT, P44 Gamma, and P44 Omicron immunosensors after incubation with mAb B38.....S8
- Figure S8.** XPS high-resolution spectra: (A) N 1s region at each fabrication stage of the P44 WT immunosensor; (B) Zn 2p region of ZnONRs; (C) O 1s region of ZnONRs.....S8
- Figure S9.** SWV signals of the immunosensor in response to varying human serum pAb concentrations and corresponding linear relationships between Δ current and the logarithm of pAb concentration: (A) P44 WT peptide; (B) P44 Gamma peptide; (C) P44 Omicron peptide.....S9
- Figure S10.** Antibody neutralization activity against WT and Omicron variants by pseudovirus assay.....S9
- Figure S11.** Parameter optimization for SWV analyses: (A) Evaluation of amplitude with frequency fixed at 40 Hz; (B) evaluation of frequency with amplitude fixed at 20 mV. The step potential was maintained at 1 mV for both experiments. Electrolyte: 5 mM K₄Fe(CN)₆/K₃Fe(CN)₆ in 0.1 M KCl.....S10
- Figure S12.** Optimization of the ZnONRs-P44 peptide-based immunosensor: (A) Effect of P44 WT peptide concentration; (B) peptide incubation time; (C) BSA concentration (% w/v); (D) BSA incubation time. The plotted signal (y-axis) represents the Δ current between the absence (control) and presence of mAb antibodies.....S10

Supporting Tables

- Table S1.** Sequence and chemical characterization data for P44 peptides and analogues..S11
- Table S2.** Atomic percentages determined by XPS analysis at each fabrication stage of the immunosensor.....S12

Supporting text

1. Experimental Section

1.1. Reagents

Zinc nitrate hexahydrate, hexamethylenetetramine (HMTA), (3-Aminopropyl) triethoxysilane (APTES), Glutaraldehyde, Bovine Serum Albumin (BSA), potassium ferricyanide and potassium ferrocyanide were purchased from Sigma-Aldrich. Potassium chloride was purchased from Labsynth. Fluorescamine was purchased from Tokyo Chemical Industry (Germany). Human Anti-SARS-CoV-2 Spike RBD (clone B38) Neutralizing mAb (CPC522A) was purchased from Cell Sciences. The following reagents were obtained through BEI Resources Repository, NIAID, NIH: Monoclonal anti-SARS-CoV S protein (similar to 540C) NR-618, Monoclonal Anti-SARS-CoV S Protein (Similar to 154C) NR-620.

1.2. Clinical Samples

A total of 45 human blood serum samples were examined in this work. Seven samples from pre-pandemic individuals, supplied by the BCRJ Cell Bank, were incorporated in this work through the approved Ethics Committee of the Universidade Federal do ABC (CAAE: 43139921.2.0000.5594). 20 serum samples from convalescent individuals with documented primary infection with SARS-CoV-2 WT strain (diagnostic confirmation by RT-PCR between March 2020) and no vaccination record, with at least 40 days since the symptom's onset. 10 serum samples from individuals vaccinated with the BNT162b2 (Pfizer–BioNTech) vaccine were obtained from individuals with no prior SARS-CoV-2 infection at least 28 days after the second dose. 4 serum samples from convalescent individuals infected with the P.1 strain (diagnostic confirmation by sequencing from May 2021) and four serum samples from convalescent individuals infected with the SARS-CoV-2 Omicron strain (diagnostic confirmation by COVID-19 quick test from January to April 2023). Written informed consent was approved by the Ethics Committee in Research of the Hospital das Clínicas da Universidade de São Paulo (HC-FMUSP CAPPesq-CAAE: 30155220.3.0000.0068) and signed by all participants. To minimize potential bias and ensure the robustness of our results, human serum samples were analyzed in random order during the experimental procedures.

1.3. ZnO Nanorods Synthesis

The ZnO nanorods were synthesized using a method previously described.¹

1.4. Electrochemical Measurements

The electrochemical analysis was conducted using an Autolab PGSTAT302N potentiostat/galvanostat with NOVA 2.1 software, provided by Metrohm. The ZnONRs electrode was considered the working electrode, a platinum (Pt) wire served as the counter electrode, and a saturated calomel electrode (SCE) was used as the reference electrode. The response measurements were conducted in 5 mM $K_4Fe(CN)_6/K_3Fe(CN)_6$ in 0.1 M KCl (pH 7.3). Cyclic voltammetry (CV) was performed from -1 to 1 V at a scan rate of 100 mV·s⁻¹. Electrochemical impedance spectroscopy (EIS) was conducted between 30 kHz and 0.1 Hz, applying 25 mV of RMS amplitude, and Square Wave Voltammetry (SWV) was carried out from -0.1 to 1 V, applying 20 mV of modulation amplitude; the frequency was set at 15 Hz, and 1 mV as step potential. All electrochemical measurements were performed in triplicate (N = 3), and average values are reported. Error bars represent the SD.

1.5. Characterization Techniques

The purified peptides were characterized by reverse-phase high-performance liquid chromatography (RP-HPLC) and mass spectrometry (LC/ESI-MS). Circular dichroism (CD) spectra were obtained using a Jasco-720 spectropolarimeter equipped with a quartz cell of 0.5 nm path length. 100 μ M of the peptide was studied in four environments: 10 mM phosphate buffer (PB), pH 7.4, and 20%, 50 %, and 70% trifluoroethanol (TFE) in this buffer. Each sample was scanned 5 times at 22°C, with spectra recorded between 190 and 260 nm. Three-dimensional structure prediction of P44 WT and its analogues was performed on the PEP-FOLD3 Server. The predicted models were then validated by Ramachandran plot analysis using PROCHECK. Field emission scanning electron microscope (FESEM), model JMS-6701F (JEOL, Tokyo, Japan), operating at 5 kV voltage, was implemented to acquire the SEM images. X-ray diffraction (XRD) pattern was acquired utilizing an X-ray spectrometer model D8 FOCUS furnished with a radiation source of Cu $K\alpha$ and operating at 40 kV and 40 mA. X-ray photoelectron spectroscopy (XPS; ThermoFisher Scientific, K-alpha+) was collected with monochromatic Al $K\alpha$ radiation. XPS data were analyzed

employing CasaXPS processing software.² Confocal laser scanning microscopy (CLSM) measurements were gathered using an LSM 710 Zeiss instrument. The samples were excited at 405 nm, and the emission was collected between 406 and 499 nm. Before the CLSM experiments, the electrodes were incubated with a solution of Fluorescamine in acetone (0.5 mg mL⁻¹) for 1 min, as previously described,¹ since Fluorescamine exhibits fluorescence upon reacting with amine groups. The mean fluorescence intensity was determined using ImageJ processing software and following the methodology described in the literature.³ For the CLSM measurements, samples were analyzed in triplicate (N = 3), and average values are reported. Error bars represent the SD.

1.6. Neutralization assay

The pseudovirus (PSDV) neutralization assay was performed as demonstrated in a previous study.⁴ In summary, the wild-type and omicron pSARS-CoV-2 S and pNL4-3 ΔEnv-NanoLuc constructs, containing the optimized SARS-CoV-2 S gene along with a human immunodeficiency virus type 1 backbone, were utilized. Viral supernatant was harvested 48 hours post-transfection and stored at -80 °C. Serially diluted serum samples (5-fold dilutions starting at 1:50) were incubated with the SARS-CoV-2 PSDV for 1 hour at 37 °C. This serum-virus mixture was then transferred onto a pre-seeded monolayer of HEK293T-hACE2 cells. After 48 hours, cells were lysed using 5× Luciferase Cell Culture Lysis reagent (Promega), and luciferase activity was quantified using the Nano-Glo system (Promega) with a luminometer (GloMax® Navigator Microplate Luminometer). The 50% inhibitory concentration (IC₅₀) for each sample was determined via nonlinear regression to evaluate its anti-SARS-CoV-2 neutralizing potency.

1.7. Statistical analysis

The variables were analyzed using the Kruskal–Wallis test, followed by Dunn’s post-hoc test for multiple comparisons. The data were analyzed using GraphPad Prism version 9.0, and $p < 0.05$ was deemed statistically significant. The Spearman rank correlation coefficient was calculated to analyze the correlation between the neutralization results from the PSDV assay and the antibody level results from the ZnONRs/p44 immunosensor, verifying the sensor's performance. Negative control serum values were excluded from calculating r - and p -values.

2. Optimization Assays

Together with the frequency, the amplitude is a crucial parameter for achieving optimal SWV analysis performance. While larger amplitudes result in higher peak intensities, excessively large amplitudes cause peak broadening and shifts in their position.⁵ On the other hand, high frequencies reduce acquisition time and enhance peak intensity; however, excessively high frequencies can produce peak widening and distortion.⁶ To assess these parameters, the effect of amplitude on current intensity was evaluated over a range of 5 to 40 mV, while maintaining the frequency at 40 Hz, and the step potential was maintained at 1 mV. As shown in Figure S11A, the best performance was achieved at 20 mV; therefore, this value was selected as the optimal amplitude. Second, the frequency effect was investigated at different values, ranging from 5 to 50 Hz, while maintaining an optimal amplitude of 20 mV and the step potential at 1 mV. As shown in Figure S11B, the optimal frequency of 15 Hz was found.

The concentration of the P44 peptide and the incubation time were investigated to optimize the performance of the immunosensor. Within the considered range of P44 peptide concentrations (5, 10, 50, and 100 ng mL⁻¹), the highest Δ_{current} was obtained for the P44 concentration of 100 ng mL⁻¹. However, the difference with 50 ng mL⁻¹ was insignificant (Figure S12A). We opted to conduct the experiments at 50 ng mL⁻¹, as it has the lowest peptide concentration and yields the most significant results. The influence of incubation time was also explored from 15 to 90 minutes (Figure S12B). The data showed that an incubation period of 45 minutes yielded optimal results.

The nonspecific adsorption of proteins present in blood serum can affect the accuracy of the immunosensor; therefore, the device surface was incubated with BSA, a commonly used blocking agent. To determine the optimal BSA concentration, non-specific interactions on the blocked surface were investigated using blood serum from a SARS-CoV-2 WT convalescent individual (1:100 v/v) (Figure S12C). The Δ_{current} obtained without blocking treatment and 0.01% BSA exhibits the most significant values compared with BSA blocking 0.1 and 1%. Therefore, this can be interpreted as poorly embeddedness for the surface and non-specific interactions. The system showed no non-specific adsorption after increasing the BSA concentration to 1%, unlike the results obtained with other BSA concentrations. Surprisingly, increasing the BSA concentration from 0.1% to 1% did not significantly affect

Δ_{current} values. The increase in values with BSA blocking at 1% may be due to excessive adsorption of BSA on the electrode surface. The results indicate that a 0.1% BSA concentration is suitable for preventing non-specific interactions in the fabricated immunosensor. The influence of BSA incubation time was also investigated in the range from 5 to 30 min (Figure S12D), and the result showed that 15 min of incubation provided the best performance.

Supporting Figures

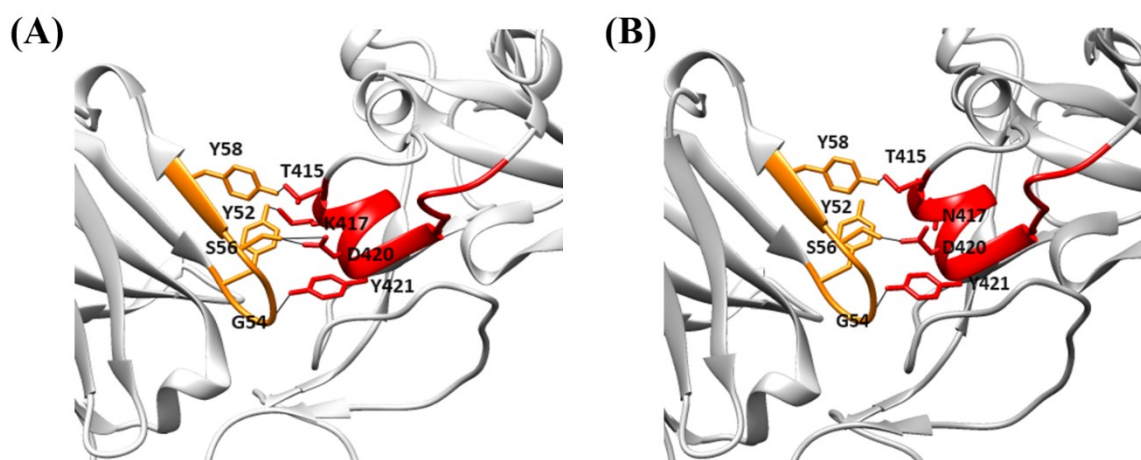


Figure S1. Structure of the B38 antibody complexed with SARS-CoV-2 RBD. (A) Wuhan RBD (PDB ID: 7BZ5), (B) Omicron RBD (PDB ID: 7XIK). The structure of the P44 peptide within the RBD structure is highlighted in red, and the residues that interact with the P44 peptide are shown in orange.

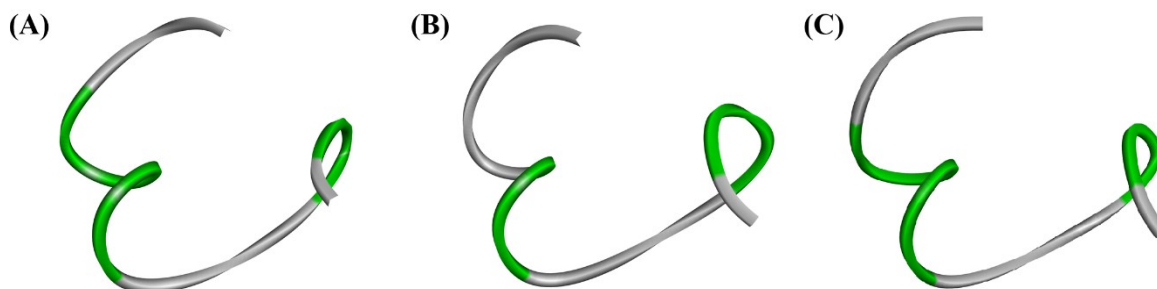


Figure S2. P44 peptides' three-dimensional structure prediction. (A) P44 WT, (B) P44 Gamma, (C) P44 Omicron. In green is shown the β -turn, and in gray are shown random coil structures.

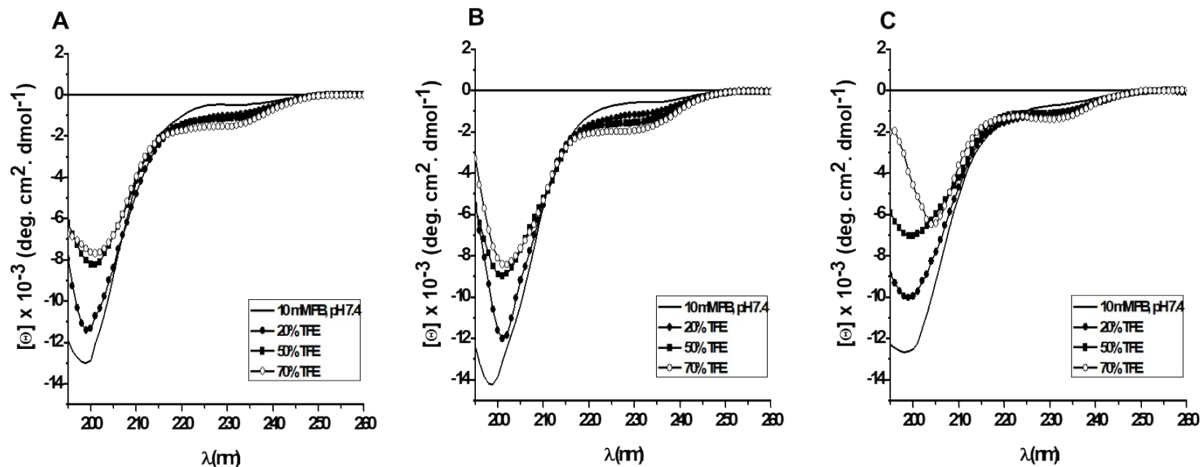


Figure S3. Circular dichroism spectra of P44 peptides: (A) WT, (B) Gamma, and (C) Omicron.

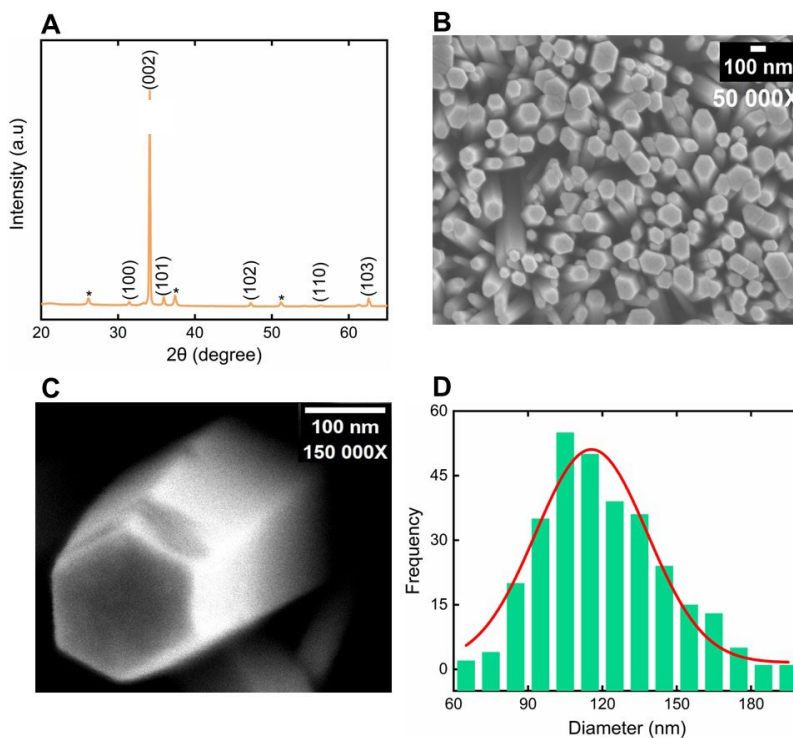


Figure S4. Crystallographic and morphological characterizations of the ZnONRs device: (A) X-ray diffraction spectra; (B) SEM image of the ZnONRs film; (C) detail of a single nanorod; (D) histogram of ZnONRs diameters.

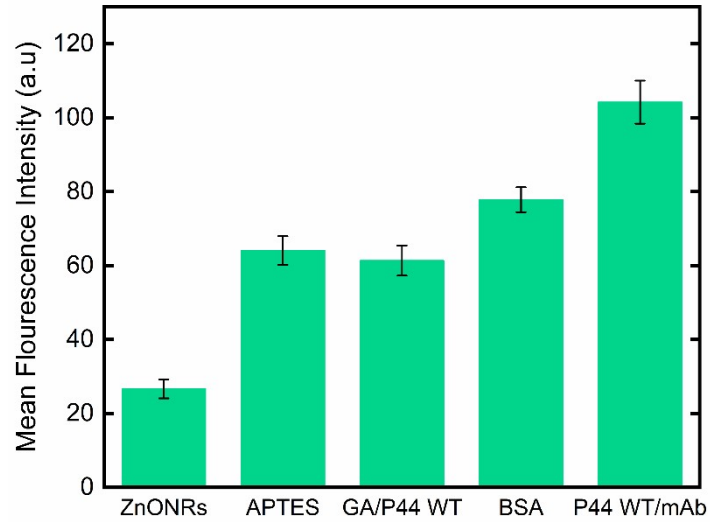


Figure S5. Mean fluorescence intensity values obtained by CLSM at each fabrication stage of the P44 WT immunosensor.

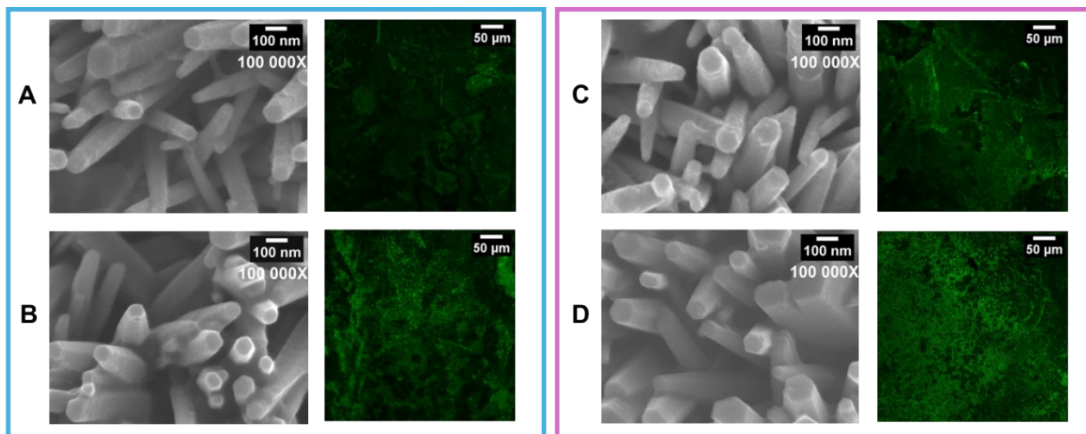


Figure S6. SEM and CLSM images at different assembly steps of P44 Gamma and P44 Omicron immunosensors: (A) ZnONRs/APTES/GA/P44 Gamma; (B) ZnONRs/APTES/GA/P44 Gamma/BSA/mAb B38; (C) ZnONRs/APTES/GA/P44 Omicron; (D) ZnONRs/APTES/GA/P44 Omicron/BSA/mAb B38.

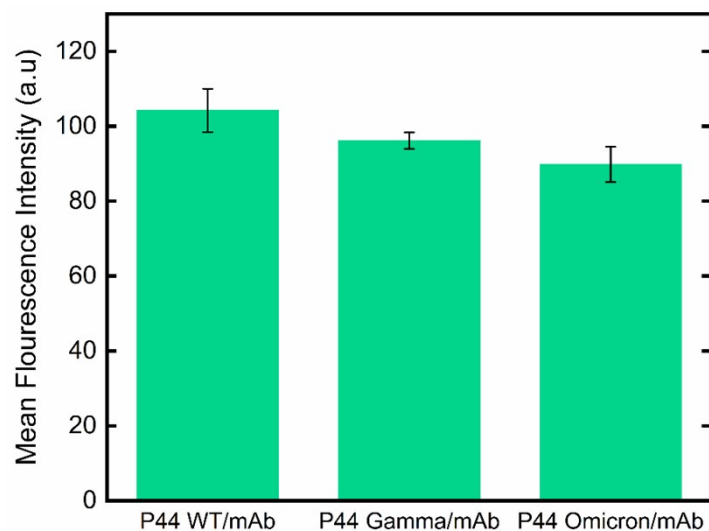


Figure S7. Comparison of mean fluorescence intensity for P44 WT, P44 Gamma, and P44 Omicron immunosensors after incubation with mAb B38.

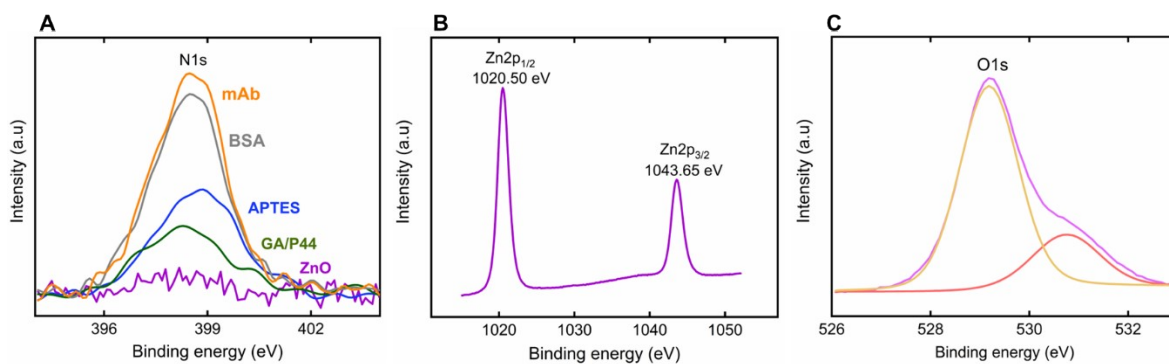


Figure S8. XPS high-resolution spectra: (A) N 1s region at each fabrication stage of the P44 WT immunosensor; (B) Zn 2p region of ZnONRs; (C) O 1s region of ZnONRs.

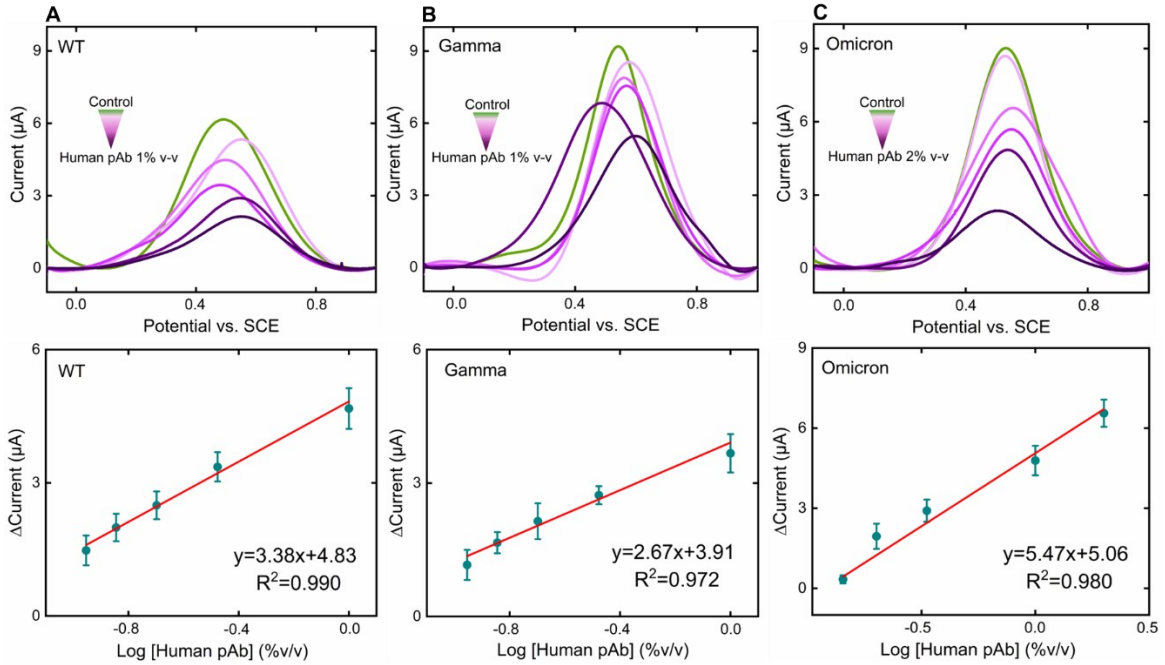


Figure S9. SWV signals of the immunosensor in response to varying human serum pAb concentrations and corresponding linear relationships between $\Delta\text{current}$ and the logarithm of pAb concentration: (A) P44 WT peptide; (B) P44 Gamma peptide; (C) P44 Omicron peptide.

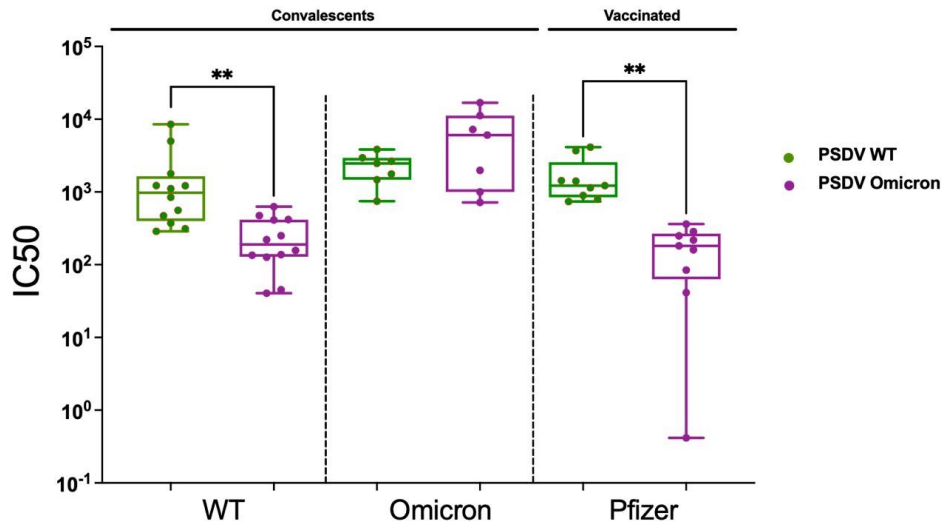


Figure S10. Antibody neutralization activity against WT and Omicron variants by pseudovirus assay.

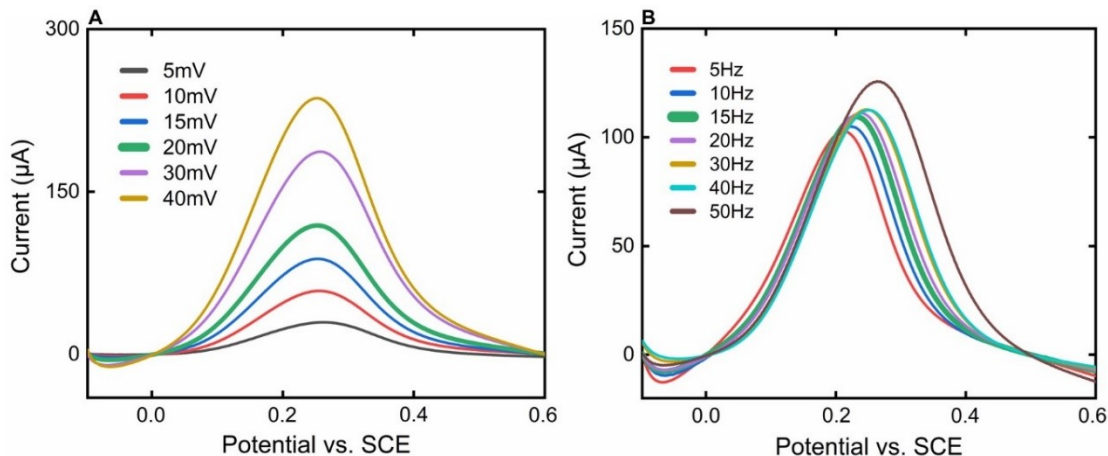


Figure S11. Parameter optimization for SWV analyses: (A) Evaluation of amplitude with frequency fixed at 40 Hz; (B) evaluation of frequency with amplitude fixed at 20 mV. The step potential was maintained at 1 mV for both experiments. Electrolyte: 5 mM $K_4Fe(CN)_6/K_3Fe(CN)_6$ in 0.1 M KCl.

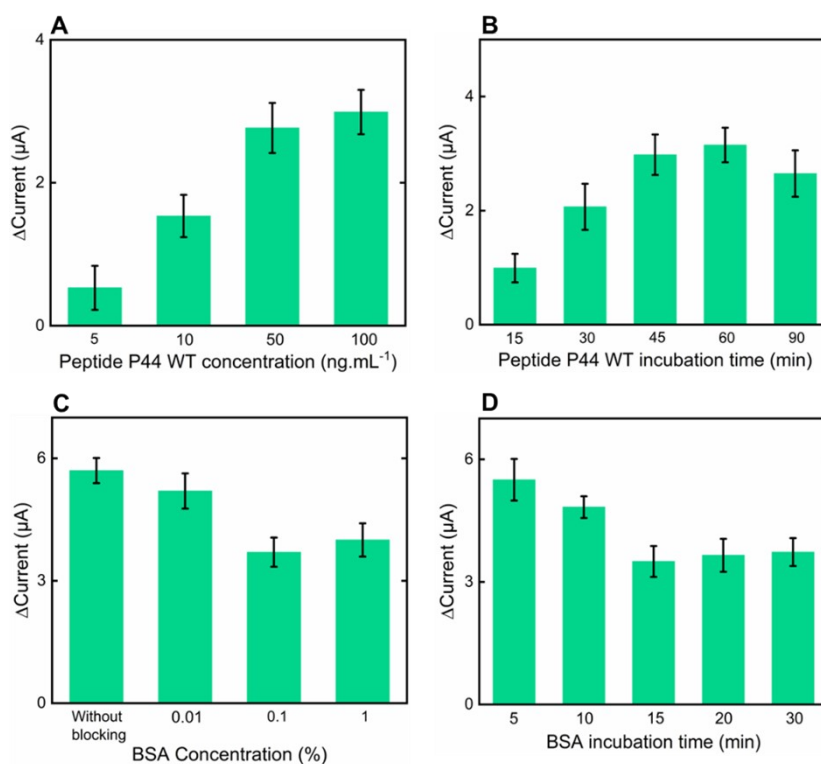


Figure S12. Optimization of the ZnONRs-P44 peptide-based immunosensor: (A) Effect of P44 WT peptide concentration; (B) peptide incubation time; (C) BSA concentration (% w/v); (D) BSA incubation time. The plotted signal (y-axis) represents the Δ current between the absence (control) and presence of mAb antibodies.

Supporting Tables

Table S1. Sequence and chemical characterization data for P44 peptides and analogues.

Sequence	Net Charge ^a (Q)	Purity ^b (%)	LC/ESI-MS calculated/measured
TGKIADYNYKLPDDF-NH ₂	0	97	1759.9/1760.0 [M+H] ⁺ 880.4/880.2 [M+2H] ²⁺ 587.3/587.2 [M+3H] ³⁺
TGTIADYNYKLPDDF-NH ₂	-1	97	1731.9/1731,9 [M+H] ⁺ 866.7/866.9 [M+2H] ²⁺ 578.3/578.2 [M+3H] ³⁺
TGNIADYNYKLPDDF-NH ₂	-1	97	1745.9/1745,8 [M+H] ⁺ 873.5/873.2 [M+2H] ²⁺ 582.6/582.6 [M+3H] ³⁺

^a Net charge at pH 7.

^b Purity was estimated by reversed-phase high-performance liquid chromatography (RP-HPLC).

Table S2. Atomic percentages determined by XPS analysis at each fabrication stage of the immunosensor.

	Samples				
	ZnONRs	ZnONRs/APTES	ZnONRs/APTES/GA/P44WT	ZnONRs/APTES/GA/P44WT/BSA	ZnONRs/APTES/GA/P44WT/BSA/mAbs
%C1S	10.04	16.65	16.3	24.09	24.4
%O1S	89.77	74.05	78.97	66.28	65.6
%N1S	0.19	5	2.63	7.77	8.26
%Si2S	0	4.31	2.1	1.86	1.74

References

1. F. A. Nunez, M. R. de A. Silva, E. M. Cilli, S. T. R. Brandão, M. Müller, D. Fischer, Q. A. Besford and W. A. Alves, *Bioelectrochemistry* 2025, 163, 108899.
2. N. Fairley, V. Fernandez, M. Richard-Plouet, C. Guillot-Deudon, J. Walton, E. Smith, D. Flahaut, M. Greiner, M. Biesinger, S. Tougaard, D. Morgan, J. Baltrusaitis, *Appl. Surf. Sci. Adv.*, 2021, 5, 100112.
3. M.H. Shihan, S.G. Novo, S.J. Le Marchand, Y. Wang, M.K. Duncan, *Biochem. Biophys. Rep.*, 2021, 25, 100916,
4. F. Schmidt, Y. Weisblum, F. Muecksch, H.H. Hoffmann, E. Michailidis, J.C.C. Lorenzi, P. Mendoza, M. Rutkowska, E. Bednarski, C. Gaebler, M. Agudelo, A. Cho, Z. Wang, A. Gazumyan, M. Cipolla, M. Caskey, D.F. Robbani, M.C. Nussenzweig, C.M. Rice, T. Hatziioannou, P.D. Bieniasz, *J. Exp. Med.* 2020, 217 (11), e20201181.
5. V. Mirceski, E. Laborda, D. Guziejewski, R.G. Compton., *Anal. Chem.*, 2013, 85 (11), 5586–5594.
6. V. Mirceski, R. Gulaboski, M. Lovric, I. Bogeski, R. Kappl, M. Hoth, Square-Wave Voltammetry: A Review on the Recent Progress, *Electroanalysis* 2013, 25 (11), 2411–2422.